Title

On-Demand Fully Enclosed Superhydrophobic-Optofluidic Devices Enabled by Microstereolithography.

Journal

Langmuir: the ACS journal of surfaces and colloids, 38(34)

Authors

Chang, Yu
Bao, Mengdi
Waitkus, Jacob
et al.

Publication Date

2022-08-30

DOI

10.1021/acs.langmuir.2c01658

Peer reviewed

HHS Public Access

Author manuscript

Langmuir. Author manuscript; available in PMC 2023 August 30.

Published in final edited form as:

Langmuir. 2022 August 30; 38(34): 10672–10678. doi:10.1021/acs.langmuir.2c01658.

On-Demand Fully Enclosed Superhydrophobic–Optofluidic Devices Enabled by Microstereolithography

Yu Chang,
Department of Mechanical Engineering, Rochester Institute of Technology, Rochester, New York 14623, United States

Mengdi Bao,
Department of Mechanical Engineering, Rochester Institute of Technology, Rochester, New York 14623, United States

Jacob Waitkus,
Department of Mechanical Engineering, Rochester Institute of Technology, Rochester, New York 14623, United States

Haogang Cai,
Tech4Health Institute and Department of Radiology, NYU Langone Health, New York, New York 10016, United States

Ke Du
Department of Mechanical Engineering, Department of Microsystems Engineering, School of Chemistry and Materials Science, and College of Health Science and Technology, Rochester Institute of Technology, Rochester, New York 14623, United States

Abstract

Superhydrophobic surface-based optofluidics have been introduced to biosensors and unconventional optics with unique advantages, such as low light loss and power consumption. However, most of these platforms were made with planar-like microstructures and nanostructures, which may cause bonding issues and result in significant waveguide loss. Here, we introduce a fully enclosed superhydrophobic-based optofluidics system, enabled by a one-step micro-stereolithography procedure. Various micro structured cladding designs with a feature size down to 100 μm were studied and a “T-type” overhang design exhibits the lowest optical loss, regardless of the excitation wavelength. Surprisingly, the optical loss of superhydrophobic-based optofluidics

Corresponding Author Ke Du – Department of Mechanical Engineering, Department of Microsystems Engineering, School of Chemistry and Materials Science, and College of Health Science and Technology, Rochester Institute of Technology, Rochester, New York 14623, United States; kdu1rit@gmail.com.

Author Contributions

All authors have commented and given approval to the final version of the manuscript. Y.C., M.B, and K.D. contributed to the design and implementation of the experiments. Y.C. and K.D. wrote the manuscript.

The authors declare no competing financial interest.

Supporting Information

The Supporting Information is available free of charge at https://pubs.acs.org/doi/10.1021/acs.langmuir.2c01658.

Measured thickness of the PTFE coating (Figure S1); micrographs of the optofluidic setup and devices (Figure S2); light transmission versus incident angle for various types of optofluidic systems (Figure S3); contact angle measurement of human plasma (Figure S4) (PDF)

is not solely decided by the solid area fraction at the solid/water/air interface, but also the cross-section shape and the effective cladding layer composition. We show that this fully enclosed optofluidic system can be used for CRISPR-labeled quantum dot quantification, intended for in vitro and in vivo CRISPR therapeutics.

Graphical Abstract

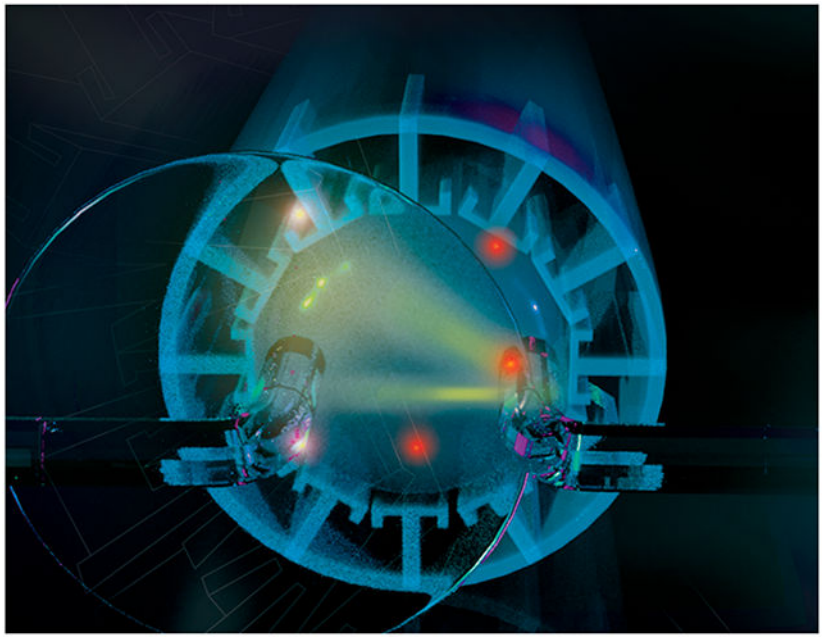

INTRODUCTION

Liquid-core optofluidic configurations, as one of the optofluidic systems, typically consist of an aqueous-core layer and a solid cladding layer.[1] The unique structure of these platforms enable a single miniaturized device to realize liquid sample holding and optical guiding functions simultaneously for applications such as fluorescence-based biosensors,[2,3] absorption spectroscopy,[4,5] and medical studies.[6,7] To achieve an efficient light guiding function, the refractive index of the core layer should be higher than the cladding layer to fulfill total internal reflection (TIR).[8] The principle of TIR is when the incident light goes from the core layer to the cladding layer with an incident angle that is less than the critical incident angle, the light would be totally reflected. There are two ways to reduce the optical loss: one is to choose the appropriate materials of core and cladding layers to maximize the difference of the refractive indexes,[9] and the other option is to utilize a complex cladding layer.[10] The latter method is more robust as the refractive index of the analyte is typically low and cannot be easily tuned.

Recently, superhydrophobic surface-based waveguide platforms have been introduced to trap air in the microstructures and nanostructures, thus reducing the effective refractive index at the interface.[11] Jonáš et al. established a tapered optical fiber waveguide coupled with a droplet standing on a super-hydrophobic surface to measure the quality factors of

individual optical resonances.[12] The superhydrophobic surface was made by spin-coated silica nanoparticles on a glass slide. However, the uniformity of such coating is difficult to control. Alternatively, high hydrophobicity was achieved by selective laser ablation on magnesium fluoride substrates.[13] However, both systems are planar-like, which limit the flexibility to vary the morphology. Previously, we developed a prototype by using sharp-tip black silicon nanostructures as a cladding layer.[14] A low loss of 0.1 dB/cm was achieved with zero incident angle, indicating that the air pockets created by the superhydrophobic nanostructures can reduce the waveguide loss. However, the black silicon nanostructures were created by conventional deep reactive ion etching on a flat and rigid substrate, causing problems for the chip packaging. Similarly, changing the morphology of the nanostructures is extremely challenging with plasma etching, preventing us to study the TIR at the interface.

To date, three-dimensional (3-D) printing technology has been widely used to build functional microstructures.[15,16] In this work, microstereolithography,[17] which is a promising technology to construct complicated 3-D structures with controllable morphology, is used to build a fully enclosed superhydrophobic-based liquid-core optofluidic device. The microstructures coated with polytetrafluoroethylene (PTFE) serve as the hydrophobic layer responsible for forming the complex cladding layer and containing air within the microstructures. The solid fraction ratio of the designed cladding layer, cross-section geometry, effective cladding composition, and excitation wavelength are studied to understand the mechanism. This work results in an optimized design guideline for the superhydrophobic cladding optofluidic platforms and is used here for quantum-dot-labeled CRISPR Cas-12a biosensing.

MATERIALS AND METHODS

Microstructured Optofluidic Design.

To create a fully enclosed optofluidic chip with microstereolithography, ultraviolet (UV) curable resin was chosen based on its high resolution and transparency. We created four different microstructures to study optical loss with a feature size down to 100 μm. Practically, the greater the number of air gaps between the created microstructures, the lower the ratio of liquid–solid contact required to form a hydrophobic layer can be. Periodic microgratings and micropins are shown in Figures 1a and 1b, respectively, with aspect ratios of ~5.7 and 8, respectively. These periodic structures have been widely used for various super-hydrophobicity applications.[11,18,19] Figure 1c shows a “T-shaped” double overhang design with super-repellent capability, since the low contact angle prevents the liquid from entering the air gap.[20] A slightly modified “umbrella” design is shown in Figure 1d, which changes the flat “T-shaped” cap to a 13.31° slope. The hydrophobicity was fulfilled by the inclined roof structures[21] and the air gaps between them. Next, the microstructures were dip-coated with PTFE (Teflon AF 6%, Chemours), followed by baking at 110 °C for 3 h to create the superhydrophobic surfaces.[22] The thickness of the coating is ~1.5 μm, as measured by a Tencor P2 profilometer (see Figure S1 in the Supporting Information). The cross-section of a liquid filled “T-shaped” structure is shown in Figure 1e. Air is sustained between the microstructures without wetting. Before coating with PTFE, the material is

hydrophilic with a static contact angle of 58° (Figure 1f). After coating, the surface exhibited superhydrophobicity with a contact angle of 120° (Figure 1g). The ultrahigh hydrophobicity that combines the superhydrophobic surface and the overhang structures creates an air gap between the microstructures with a center-to-center distance of 2.8 mm (Figure 1h), which is far greater than the distance in optofluidic design (70 μm). The droplet could be "repelled" because of the considerable vertical component of the surface tension on the overhangs and the air layer creates a light guiding function. As shown in Figure 1i, TIR at the solid/water/air interface of the "T-shape" channel is achieved, as denoted by the yellow arrow, where light is reflected back into the liquid core with an incident angle of ~35°. As a fully enclosed optofluidic system, the liquid inlet and outlet were created during the printing step, thus avoiding leaking issues and forming a working device, as shown in Figure 1j.

Transmission Measurements.

The measurement setup is shown in Figure 2a. An optical fiber-coupled LED laser (emitter diameter: 1 mm, Thorlab, Model M00559094) is aligned with the optofluidic chip, which is placed on a 3-D stage (Thorlabs, Model MBT616D). The fiber is connected to a UV lens where the incident angle can be tuned. The outlet of the optofluidic chip is connected to a filter (Catalog No. FB610-10) and another optical fiber to collect the light signal and send it to a spectrometer (Model FLMS16493). The incident angle was fixed at 5° (max transmission intensity) for all samples and tested for four different excitation wavelengths: 405, 490, 595, and 1,100 nm. More images of the optical setup and optofluidic chips are shown in Figure S2 in the Supporting Information.

CRISPR-Cas12a Sensing with the Optofluidic Device.

The CRISPR-Cas complexes were first prepared by mixing 1 μL of binding buffer, 62.5 nM of biotinylated single-stranded DNA probes, and 9.5 μL of nuclease free water. After adding the target DNA, the mixture was immediately activated and incubated at 37 °C for 2 h. Next, the reaction product was mixed with 1.68 nM of streptavidin-coated quantum dots at room temperature for 30 min. Following that, the mixture was incubated with antifluorescein-coated magnetic beads at room temperature for 30 min, allowing the intact probe-quantum dot conjugate to react with magnetic beads. The newly formed magnetic bead-probe-quantum dot conjugates were then isolated and removed from the desired supernatant, which contained the quantum dots with degraded probes, because of the CRISPR-Cas complex. Finally, the supernatant was collected, diluted, and added into the optofluidic device.

RESULTS AND DISCUSSION

As shown in Figures 2b-e, for all the measurements, the "T-shaped" sample shows the highest transmission, regardless of the excitation wavelength. The flat sample (without any microstructures) shows a ~20% lower transmission of the light beam than the "T-shaped" sample, followed by the "umbrella" sample, the micrograting, and the micropins. Based on the 3-D ray tracing analysis,[23] the cladding layer thickness should be smaller than 15% of the core diameter to ensure the light rays travel primarily within the core. As the diameter of the core is 6 mm, we calculated that the thickness of the cladding layer required is 900

μm, theoretically. Within the range of the required thickness (900 μm), various geometries were tested to clarify the light-guiding performance in terms of different solid fractions. The calculated solid fractions are as follows: 29.6% for micrograting, 42% for micropins, 41.2% for flat surface, 86.4% for "umbrella" structures, and 36.9% for "T-shaped" structures. Since Teflon is very thin, compared to the printing material, it is neglected during calculation. Note that, for the flat optofluidic device, the solid substrate is solely the 400 μm wall within the required cladding thickness of 900 μm. Based on the theory of TIR, a lower solid fraction for the cladding layer can reduce the optical loss. Thus, we expected the micrograting should provide the highest transmission, followed by the "T-shaped" and flat samples. As shown in Figure 2, "T-shaped" and flat samples always show the highest transmission among all the designs, which agree with our theoretical prediction. However, the measured transmission for micrograting and micropins are significantly lower. This is a result of part of the microstructures collapsing following the PTFE coating.[24] On the other hand, the mechanical stability of "T-shaped" and "umbrella" microstructures are much higher, thus providing improved containment of the liquid in the core while showing better optofluidic performance. During the entire optofluidic measurement (~1 h), we did not observe the dissolution of the air gap. We also tested light transmission versus incident angle for all the channels, showing that "T-shaped" microstructures are always more efficient than other channels with an incident angle up to 15° (see Figure S3 in the Supporting Information).

We further study the light-guiding capabilities of the microstructures based on the solid cladding thickness, light refraction, and macroscopic scattering. Figure 3a shows the transmission intensity of a flat optofluidic chip with a wall thickness of 400 and 600 μm, respectively. A 200 μm increase of the wall thickness significantly reduces the light transmission. With a zero incident angle, the light transmission for the 600 μm sample is ~4 times less than that of the 400 μm sample, because the solid fraction in the effective cladding layer absorbs the light. To reduce the optical loss, the solution, as described above, is to reduce the wall thickness, which is why the 400 μm thick flat optofluidic chip demonstrates good performance, even without microstructure-aided superhydrophobicity. There are two ways to reduce the solid fraction within the cladding layer to enhance the light-guiding performance. One is to produce the transverse pores within the current structures, which has been used to modify the refractive indices for thin films[25] and coatings.[26] The other one is to reduce the feature size directly, which was investigated in the following experiments. To further shrink the overall size of the optofluidics, "T-shape" microstructures must be used as for the flat channel, the thin cladding layer cannot support the mechanical stresses.

As shown in Figure 3b, the majority of the incident light beam (blue arrow) is absorbed by the solid wall while part of the light is reflected by the air cladding (purple arrow). Importantly, another part of the light is refracted and then reflected due to the combination of thin solid and air cladding (red arrow). Therefore, we demonstrated an ideal super-hydrophobicity-based optofluidic configuration by minimizing the microstructure cap thickness and increasing the air cladding layer thickness, enabling an "air-mirror"[27] at the solid/water/air interface. As a result, most of the light intensity will be reflected, because of the thick air-cladding layer.

The next factor investigated was how the cross-sectional shape of the liquid core can affect the light guiding as it can change the refraction of the light at the interface of solid/water/air. During the light propagation, the light rays will split into various refracted beams, and such a multipath phenomenon would lead to a nonlinear intensity. Ideally, a light guiding device consisting of a round core layer and a round cladding layer can better confine the refracted light rays in the center, as well as more of the linear light intensity.[23] In Figure 3c, several "T-shaped" devices were produced by varying the round shape smoothness at the interface between the core and cladding. Every device has nearly the same core layer volume, as well as height of the microstructures. The solid fractions for T-1, T-3, and T-4 are similar at 37.5%, 38.4%, and 40%, respectively. While T-2 and T-4 have comparable solid fractions, which are 28.5% and 30.8%, respectively.

T-1 has the best performance among the various structure designs. At a zero degree incident angle, the light transmission is at least 3.5 times better than the other designs. This is because the cross-section of T-1 is closest to a round shape and the width of the cap for T-1 is wider than the others, except for T-2. The wider the T-cap, the more "air-mirrors" created within the device. Therefore, more light can be reflected or partially reflected by the air cladding or air-thin solid mixed cladding layer. On the other hand, the core geometry of the T-2 cross-section is less round than that of T-1, meaning less light is reflected back to the liquid core, regardless of the greater width. T-3, T-4, and T-5 also show more loss since they have narrower caps, resulting in less partial refraction. Ignoring the difference in the cap widths when compared to T-1 and T-2, the overhang structures within T-3, T-4, and T-5 are longer than the other designs, which may cause greater intensity loss. Although the overhang structure provides the extra support necessary to hold the liquid, it still must be controlled at a reasonable thickness to avoid over increasing the solid substrate portion within the effective cladding layer. Lastly, T-5 has the lowest transmission due to a less circular cross-sectional geometry in addition to the longer length of the T-caps within the effective cladding thickness. These combined alterations to the microstructure design lead to a greater intensity loss caused by the solid substrate, and a narrower width of the T-caps.

Figure 4 shows the application of the various designed optofluidic chips for fluorescence detection. Carboxyl quantum dots (size: 15–20 nm; Thermo Fisher Scientific) were prepared with a concentration ranging from 0.1 nM to 6.25 nM. The excitation wavelength was fixed at 405 nm with an incident angle of 18°. Three scans were averaged for each measurement with an integration time set at 100 ms. The uncorrected fluorescence spectra for the 1.6 nM quantum dots (211 μL) in different optofluidic chips are shown in Figure 4a, matching the trend from the transmission tests. The peak intensity for the "T-shaped" device is ~2 times higher than the flat device, as enabled by the TIR from air-cladding and air-thin solid mixed cladding. The integrated fluorescence intensity of various quantum dot concentrations are shown in Figure 4b, where the "T-shaped" structure shows the best performance, and the measured intensity linearly increases with the concentration.

Lastly, we show that the optofluidic device can combine with a CRISPR-Cas12a system for the detection of target DNA.[28,29] As shown in Figure 5a, with the presence of target DNA, the single-stranded DNA probes are denatured by the CRISPR complex, thus leaving the quantum dots unconjugated in the solution.[30] On the other hand, without

target DNA, the single-stranded DNA probes are intact, allowing the quantum dots to be captured by the magnetic beads and extracted from the necessary supernatant. The CRISPR-activated quantum dots remaining in the supernatant are then quantitatively evaluated by our optofluidics system. During the experiment, we did not observe the absorption of tested biomolecules and quantum dots. We set the quantum dot concentration at 1.68 nM and vary the DNA target concentration. As shown in Figure 5b, the integrated fluorescence intensity linearly increases with the increase in DNA target concentration from 0.1 to 1 nM. On the other hand, the sample without target input (NTC) has a lower signal than the 0.1 nM sample of target DNA strands.

Different from solid core waveguides,[31] this fully enclosed optofluidic system can efficiently collect the fluorescence signal of the CRISPR cleavage products in the liquid core, holding immense prospect for optogenetic therapy to deliver reagents locally or within specific tissues to treat various diseases such as sepsis,[32] cancer,[33] and neurological diseases.[34] Leveraging the high resolution of stereolithography, the “T-shaped” structures can be fabricated with a smaller dimension for microsurgery while still providing efficient light transmission.[35] We also show that the “T-shaped” microstructures can prevent the wetting of human plasma (Figure S4 in the Supporting Information), which is a huge advantage of reducing biofouling issues for in vivo applications.[36] In the future, microvalves, micropumps, and LED light sources can also be 3-D printed and integrated with our optofluidics system as a single unit for sample loading, sensing, and treatment.[37,38]

CONCLUSIONS

In summary, different designed geometries of superhydrophobic-based optofluidic devices were built by high-resolution stereolithography techniques and examined via transmission and fluorescence measurements. The solid fraction within the range of theoretically required cladding thickness and the smoothness of the core’s cross-section were investigated to optimize our fully enclosed optofluidic devices. Among all the designs, the “T-shaped” optofluidic chip with a wide and thin T-cap, a short overhang length, and a round cross-section of the core shows the best performance with all the excitation wavelengths we tested, which agrees with our theoretical model. This “T-shape” optofluidic system was used to quantify a quantum-dot-based CRISPR-Cas12 assay, thus establishing a novel technology capable of developing the next generation of CRISPR therapeutics for in vivo applications.

Supplementary Material

Refer to Web version on PubMed Central for supplementary material.

ACKNOWLEDGMENTS

The authors thank Sunghwan Bae and Mary Nguyen from RIT for the schematic design and Henry Yuqing for taking the SEM images.

Funding

This work was supported by the National Institute of General Medical Sciences of the National Institutes of Health, under Award No. R35GM142763, Burroughs Wellcome Fund (No. 1019955), and the UNYTE Pipeline-to-Pilot

grant (No. 37161). The content is solely the responsibility of the authors and does not necessarily represent the official views of the National Institutes of Health.

ABBREVIATIONS

TIR	total internal reflection
PTFE	polytetrafluoroethylene

REFERENCES

(1). Minzioni P; Osellame R; Sada C; Zhao S; Omenetto FG; Gylfason KB; Haraldsson T; Zhang Y; Ozcan A; Wax A; et al. Roadmap for optofluidics. J. Opt 2017, 19 (9), 093003.

(2). Jakubowski K; Kerkemeyer W; Perret E; Heuberger M; Hufenus R Liquid-core polymer optical fibers for luminescent waveguide applications. Mater. Des 2020, 196, 109131.

(3). Wei L; Tian Y; Yan W; Cheung K; Ho D Liquid-core waveguide TCSPC sensor for high-accuracy fluorescence lifetime analysis. Anal. Bioanal. Chem 2019, 411 (16), 3641–3652. [PubMed: 31037372]

(4). Robles T; Paige D; Anastasio C Lens-coupled liquid core waveguide for ultraviolet-visible absorption spectroscopy. Rev. Sci. Instrum 2006, 77 (7), 073103.

(5). Nissen M; Doherty B; Hamperl J; Kobelke J; Weber K; Henkel T; Schmidt MA UV Absorption Spectroscopy in Water-Filled Antiresonant Hollow Core Fibers for Pharmaceutical Detection. Sensors 2018, 18 (2), 478. [PubMed: 29415468]

(6). Kottke D; Burckhardt BB; Breitkreutz J; Fischer B Application and validation of a coaxial liquid core waveguide fluorescence detector for the permeation analysis of desmopressin acetate. Talanta 2021, 226, 122145. [PubMed: 33676696]

(7). Meister J; Franzen R; Eyrich G; Bongartz J; Gutknecht N; Hering P First clinical application of a liquid-core light guide connected to an Er:YAG laser for oral treatment of leukoplakia. Lasers Med. Sci 2010, 25 (5), 669–673. [PubMed: 20393767]

(8). Morhart TA; Read ST; Wells G; Jacobs M; Rosendahl SM; Achenbach S; Burgess IJ Micromachined multigroove silicon ATR FT-IR internal reflection elements for chemical imaging of microfluidic devices. Anal. Methods 2019, 11 (45), 5776–5783.

(9). Liu Z; Zhang ZF; Tam H-Y; Tao X Multifunctional Smart Optical Fibers: Materials, Fabrication, and Sensing Applications. Photonics 2019, 6 (2), 48.

(10). Fesenko VI; Tuz VR; Shulika OV; Sukhoivanov IA Dispersion properties of Kolakoski-cladding hollow-core nanophotonic Bragg waveguide. Nanophotonics 2016, 5 (4), 556–564.

(11). Asawa K; Kumar S; Huang Y; Choi C-H Guiding light via slippery liquid-infused porous surfaces. Appl. Phys. Lett 2021, 118 (9), 091602.

(12). Jonáš A; Yalizay B; Akturk S; Kiraz A Free-standing optofluidic waveguides formed on patterned superhydrophobic surfaces. Appl. Phys. Lett 2014, 104 (9), 091123.

(13). Jonáš A; Karadag Y; Mestre M; Kiraz A Probing of ultrahigh optical Q-factors of individual liquid microdroplets on superhydrophobic surfaces using tapered optical fiber waveguides. J. Opt. Soc. Am. B 2012, 29 (12), 3240–3247.

(14). Du K; Wathuthanthri I; Ding J; Choi C-H Super-hydrophobic waveguide: Liquid-core air-cladding waveguide platform for optofluidics. Appl. Phys. Lett 2018, 113 (14), 143701.

(15). Gaxiola-López JC; Lara-Ceniceros TE; Silva-Vidaurri LG; Advincula RC; Bonilla-Cruz J 3D Printed Parahydrophobic Surfaces as Multireaction Platforms. Langmuir 2022, 38 (25), 7740–7749. [PubMed: 35687828]

(16). Shi W; Cheng X; Cheng K Gecko-Inspired Adhesives with Asymmetrically Tilting-Oriented Micropillars. Langmuir 2022, 38 (29), 8890–8898. [PubMed: 35830463]

(17). You S; Miller K; Chen S Chapter 1 Microstereolithography. In Biofabrication and 3D Tissue Modeling; The Royal Society of Chemistry: London, 2019; pp 1–21.

(18). Yoon Y; Kim D; Lee J-B Hierarchical micro/nano structures for super-hydrophobic surfaces and super-lyophobic surface against liquid metal. Micro Nano Syst. Lett 2014, 2 (1), 3.

(19). Misiiuk K; Lowrey S; Blaikie R; Juras J; Sommers A Study of Micro- and Nanopatterned Aluminum Surfaces Using Different Microfabrication Processes for Water Management. Langmuir 2022, 38 (4), 1386–1397. [PubMed: 35050636]

(20). Liu TL; Kim C-JC Turning a surface superrepellent even to completely wetting liquids. Science 2014, 346 (6213), 1096–1100. [PubMed: 25430765]

(21). Hizal F; Rungraeng N; Lee J; Jun S; Busscher HJ; van der Mei HC; Choi C-H Nanoengineered Superhydrophobic Surfaces of Aluminum with Extremely Low Bacterial Adhesivity. ACS Appl. Mater. Interfaces 2017, 9 (13), 12118–12129. [PubMed: 28291321]

(22). Cho SH; Godin J; Lo Y-H Optofluidic Waveguides in Teflon AF-Coated PDMS Microfluidic Channels. IEEE Photonics Technol. Lett 2009, 21 (15), 1057–1059. [PubMed: 20729984]

(23). Kraiczek KG; Mannion J; Post S; Tsupryk A; Raghunathan V; Brennen R; Zengerle R Micromachined Fused Silica Liquid Core Waveguide Capillary Flow Cell. Anal. Chem 2016, 88 (2), 1100–1105. [PubMed: 26691325]

(24). Du K; Jiang Y; Liu Y; Wathuthanthri I; Choi CH Manipulation of the Superhydrophobicity of Plasma-Etched Polymer Nanostructures. Micromachines (Basel) 2018, 9 (6), 304. [PubMed: 30424237]

(25). Hulkkonen HH; Salminen T; Niemi T Block Copolymer Patterning for Creating Porous Silicon Thin Films with Tunable Refractive Indices. ACS Appl. Mater. Interfaces 2017, 9 (37), 31260–31265. [PubMed: 28195697]

(26). Bao L; Ji Z; Wang H; Chen R Hollow Rodlike MgF2 with an Ultralow Refractive Index for the Preparation of Multifunctional Antireflective Coatings. Langmuir 2017, 33 (25), 6240–6247. [PubMed: 28602095]

(27). Dervisevic E; Voelcker NH; Risbridger G; Tuck KL; Cadarso VJ High-Aspect-Ratio SU-8-Based Optofluidic Device for Ammonia Detection in Cell Culture Media. ACS Sensors 2020, 5 (8), 2523–2529. [PubMed: 32666799]

(28). Chen JS; Ma E; Harrington LB; Da Costa M; Tian X; Palefsky JMDoudna JA CRISPR-Cas12a target binding unleashes indiscriminate single-stranded DNase activity. Science 2018, 360 (6387), 436–439. [PubMed: 29449511]

(29). Broughton JP; Deng X; Yu G; Fasching CL; Servellita V; Singh J; Miao X; Streithorst JA; Granados A; Sotomayor-Gonzalez A; et al. CRISPR–Cas12-based detection of SARS-CoV-2. Nat. Biotechnol 2020, 38 (7), 870–874. [PubMed: 32300245]

(30). Bao M; Jensen E; Chang Y; Korensky G; Du K Magnetic Bead-Quantum Dot (MB-Qdot) Clustered Regularly Interspaced Short Palindromic Repeat Assay for Simple Viral DNA Detection. ACS Appl. Mater. Interfaces 2020, 12 (39), 43435–43443. [PubMed: 32886473]

(31). Wang L; Zhong C; Ke D; Ye F; Tu J; Wang L; Lu Y Ultrasoft and Highly Stretchable Hydrogel Optical Fibers for In Vivo Optogenetic Modulations. Adv. Opt. Mater 2018, 6 (16), 1800427.

(32). Lim K; Kim T.-h.; Trzeciak A; Amitrano AM; Reilly EC; Prizant H; Fowell DJ; Topham DJ; Kim M In situ neutrophil efferocytosis shapes T cell immunity to influenza infection. Nat. Immunol 2020, 21 (9), 1046–1057. [PubMed: 32747818]

(33). Fan N; Bian X; Li M; Chen J; Wu H; Peng Q; Bai H; Cheng W; Kong L; Ding S; et al. Hierarchical self-uncloaking CRISPR-Cas13a–customized RNA nanococoons for spatial-controlled genome editing and precise cancer therapy. Sci. Adv 2022, 8 (20), eabn7382. [PubMed: 35584220]

(34). Park H; Oh J; Shim G; Cho B; Chang Y; Kim S; Baek S; Kim H; Shin J; Choi H; et al. In vivo neuronal gene editing via CRISPR–Cas9 amphiphilic nanocomplexes alleviates deficits in mouse models of Alzheimer's disease. Nat. Neurosci 2019, 22 (4), 524–528. [PubMed: 30858603]

(35). Zhao X; Shi Y; Pan T; Lu D; Xiong J; Li B; Xin H In Situ Single-Cell Surgery and Intracellular Organelle Manipulation Via Thermoplasmonics Combined Optical Trapping. Nano Lett. 2022, 22 (1), 402–410. [PubMed: 34968073]

(36). Guo Y; Chen C; Feng J; Wang L; Wang J; Tang C; Sun X; Peng H An Anti-Biofouling Flexible Fiber Biofuel Cell Working in the Brain. Small Methods 2022, 6 (5), 2200142.

(37). Alvarez-Braña Y; Etxebarria-Elezgarai J; Ruiz de Larrinaga-Vicente L; Benito-Lopez F; Basabe-Desmonts L Modular micropumps fabricated by 3D printed technologies for polymeric microfluidic device applications. Sens. Actuators B: Chem 2021, 342, 129991.

(38). Forouzandeh F; Ahamed NN; Zhu X; Bazard P; Goyal K; Walton JP; Frisina RD; Borkholder DA A Wirelessly Controlled Scalable 3D-Printed Microsystem for Drug Delivery. Pharmaceuticals (Basel) 2021, 14 (6), 538. [PubMed: 34199855]

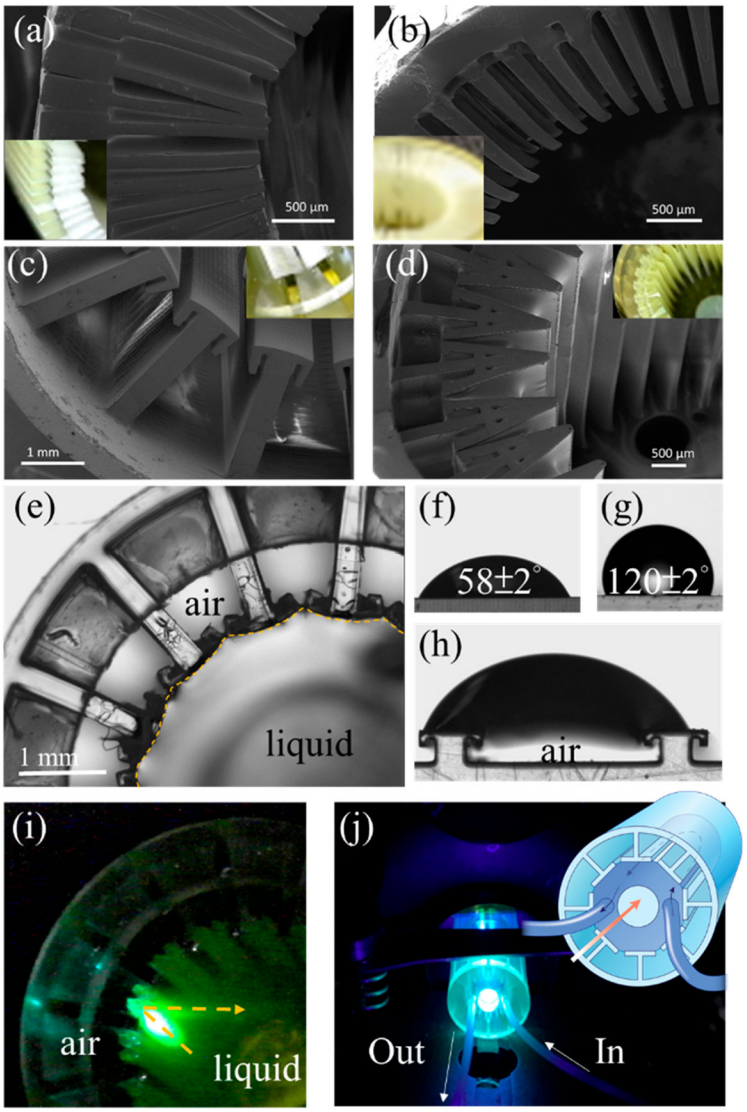

Figure 1.

SEM image and optical micrograph of (a) micrograting structures, (b) micropins structures, (c) “T-shaped” structures, and (d) “umbrella” structures. (e) Cross-section of a “T-shaped” optofluidic device filled with water in the core. The solid/water/air interface is labeled with a dashed yellow line. (f, g) The static water contact angle measurement of a flat sample before Teflon AF coating (panel (f)) and after Teflon AF coating (panel (g)). (h) Photographs showing the droplet supported by two “T-shaped” structures with a wide gap. (i) Light beam reflected at the solid/water/air interface with an incident angle of 35°. (j) Micrograph of a working optofluidic platform with the light sharing the same path with the liquid core. Liquid is pumped into the liquid core through the embedded microtubing. The fluid flow directions in the device are depicted in the inset.

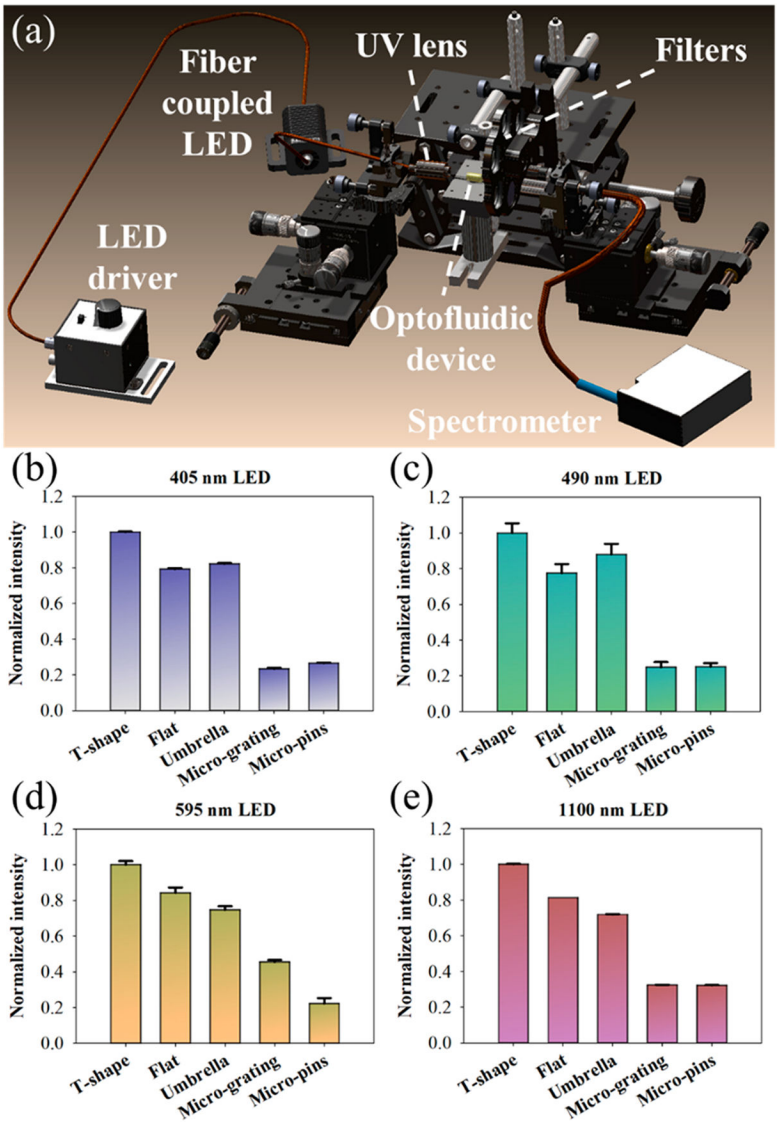

Figure 2.

(a) Schematic of the setup for optical measurements. Normalized light transmission of different optofluidic chips with an excitation at (b) 405, (c) 490, (d) 595, and (e) 1100 nm. The error bars represent the standard deviation for each respective sample. Every data point represents the average of three measurements.

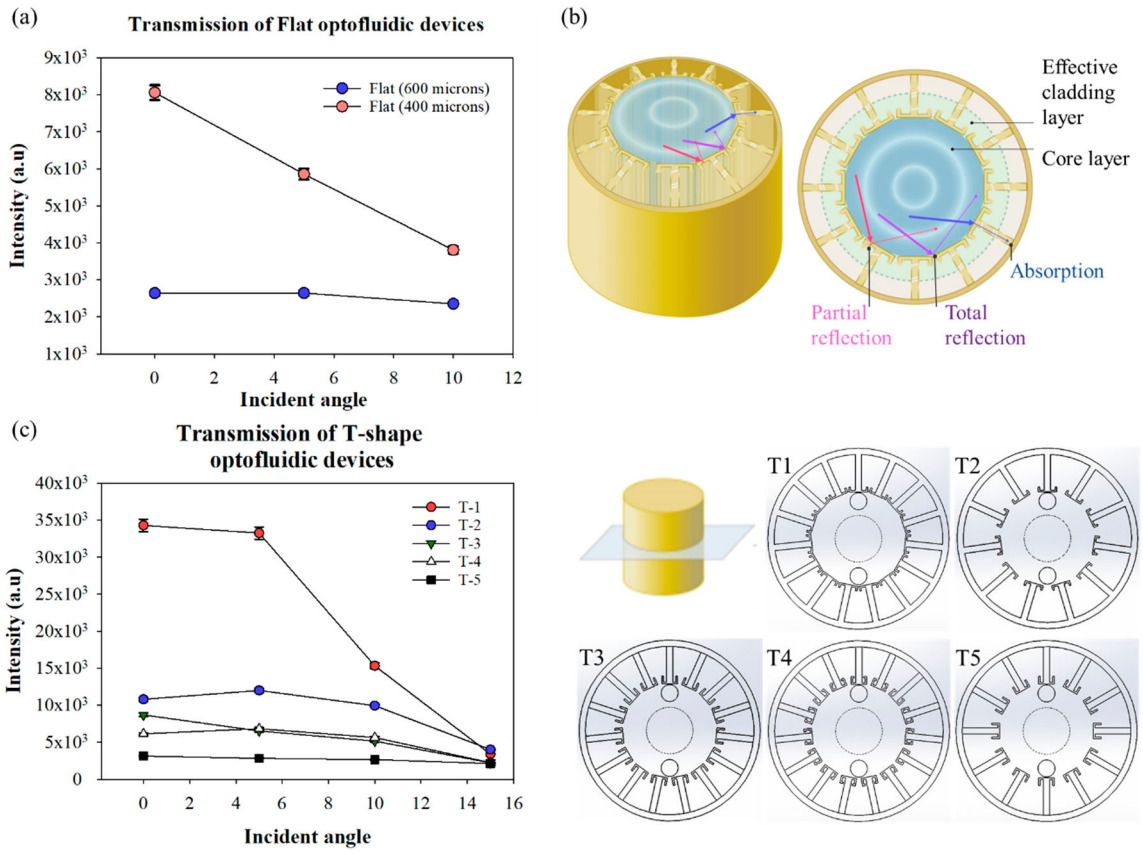

Figure 3.

(a) Transmission measurements of a flat optofluidic chip with a solid cladding thickness of 400 and 600 μm, respectively. (b) Schematic of the solid/water/air interface to explain the loss mechanism. (c) Transmission measurements of various “T-shaped” structures and incident angles as T-1 shows the best performance. Every data point represents the average of three measurements.

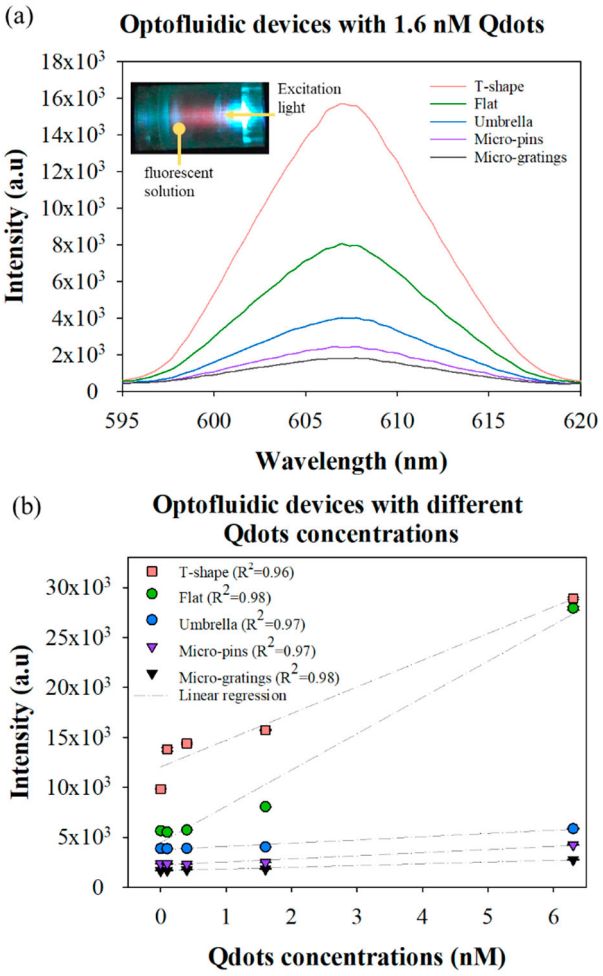

Figure 4.

(a) Uncorrected fluorescence emission spectrum of various optofluidic platforms by inputting 1.6 nM quantum dots. The inset is a photograph of a fluorescent solution (red) within the device. The light traveled from right to left. (b) Integrated fluorescence signal in the optofluidic platforms by increasing the quantum concentrations from 0 to 6.3 nM. Every data point represents the average of three measurements.

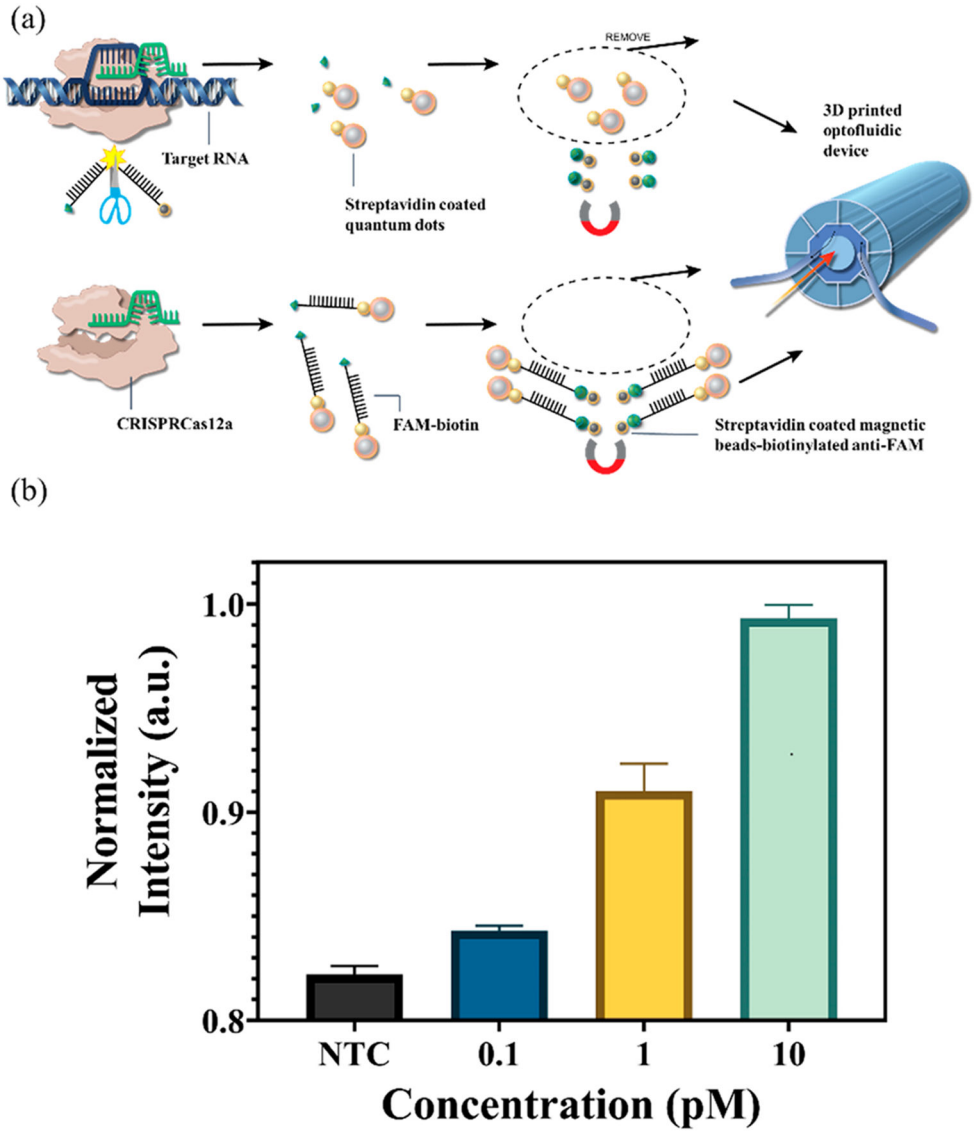

Figure 5.

(a) Procedure of clustered regularly interspaced short palindromic repeat (CRISPR) in conjunction with associated proteins (Cas) for simple and sensitive nucleic acid detection. (b) Fluorescence intensities of samples with DNA target input of 0.1, 1, and 10 nM. Negative control (without target) is labeled as NTC. Every data point represents the average of three measurements.